Mineralium Deposita (2023) 58:223–241
https://doi.org/10.1007/s00126-022-01117-z

ARTICLE

Archetypal Au-bearing silica sinter from the Miocene Milestone deposit, Idaho, USA

Emily R. Fenner[1] · Matthew E. Brueseke[1] · Barry J. Shaulis[2]

Received: 25 April 2022 / Accepted: 25 April 2022 / Published online: 20 May 2022

Abstract

The Milestone silica sinter defines a mid-Miocene epithermal paleosurface that is adjacent to the DeLamar Ag–Au deposit in the Silver City District (SCD), Idaho. Milestone, DeLamar, and other SCD deposits (e.g., War Eagle and Florida mountain) are part of the same suite of ~ 17–14 Ma bonanza Au–Ag deposits associated with volcanism that demarcates the onset of the Yellowstone hotspot across the northern Great Basin (USA). Geologic mapping of the Main Knob of Milestone reveals five lithofacies in the paleosurface: matrix-supported breccia, clast-supported breccia (cross-cut by near-vent silica gel), silica sinter and geyserite, and bioformations. The facies are indicative of a paleohot spring, typical of active hot spring environments. Electrum microparticles occur in dark-gray to black bands in the sinter, which resemble high-grade ore-bearing ginguro bands in epithermal veins. Transect and spot trace element analyses by LA-ICP-MS show that these sinter bands are associated with metal(loid) concentrations (0.03–291 ppm Au and 0.19–28,400 ppm Ag). The metal-rich bands show textures that reflect the transportation and deposition of Au-rich particles. These textures, coupled with a lack of compositional variation across the different sinter facies (distance from hot springs vent), suggest that the Au-rich particles formed at depth and were then transported to the surface. This occurrence of precious metals in Milestone sinter likely indicates metal-bearing veins at depth, along faults and other structural weaknesses that channeled the liquid to the surface. Milestone sinter, first recognized by Lindgren, is analogous to those of the Yellowstone and Taupo Volcanic Zone geothermal systems.

Keywords Hot springs · Epithermal · Precious metals · Nanoparticles · Paleoenvironment reconstruction

Introduction

The Milestone deposit is part of the Silver City District (SCD), located in the Owyhee Mountains (Idaho, USA; Fig. 1). The district includes the DeLamar epithermal deposit, 3 km southeast of Milestone, which produced 0.4 Moz Au and 5.9 Moz Ag from 726 kt of ore during the period 1891–1913; open-pit mining from 1977 to 1998 produced a further 0.625 Moz Au and 45 Moz Ag (Gustin et al. 2019). The district is the birthplace of several modern ideas about epithermal precious metal deposits (Lindgren 1900). Silica sinters at Milestone were identified by Lindgren (1900), who called them "spring deposits," and his observations influenced his subsequent epithermal model (Lindgren 1933). For this reason, the deposit is a significant geoheritage site.

Our study presents evidence on the metal(loid) enrichment in the Milestone silica sinters, based on characterization of the preserved depositional facies. We studied textures and mineralogy and conducted in situ elemental analyses of the Milestone Main Knob sinter. These data provide geological constraints on how the Milestone deposit formed and allow a reconstruction of the paleoenvironments preserved in the depositional facies.

Silica sinters

Epithermal Au–Ag mineralization is commonly associated with silica sinter where the paleosurface is preserved (Sillitoe 1989; 2015). In these systems, the metal(loid)s and their ligands are transported by hydrothermal fluids that form Au and Ag deposits (Hedenquist and Lowenstern 1994; John

Editorial handling: H. E. Frimmel

✉ Matthew E. Brueseke
brueseke@ksu.edu

[1] Department of Geology, Kansas State University, 108 Thompson Hall, Manhattan, KS 66506, USA

[2] Trace Element and Radiogenic Isotope Lab, Department of Geosciences, University of Arkansas, Fayetteville, USA

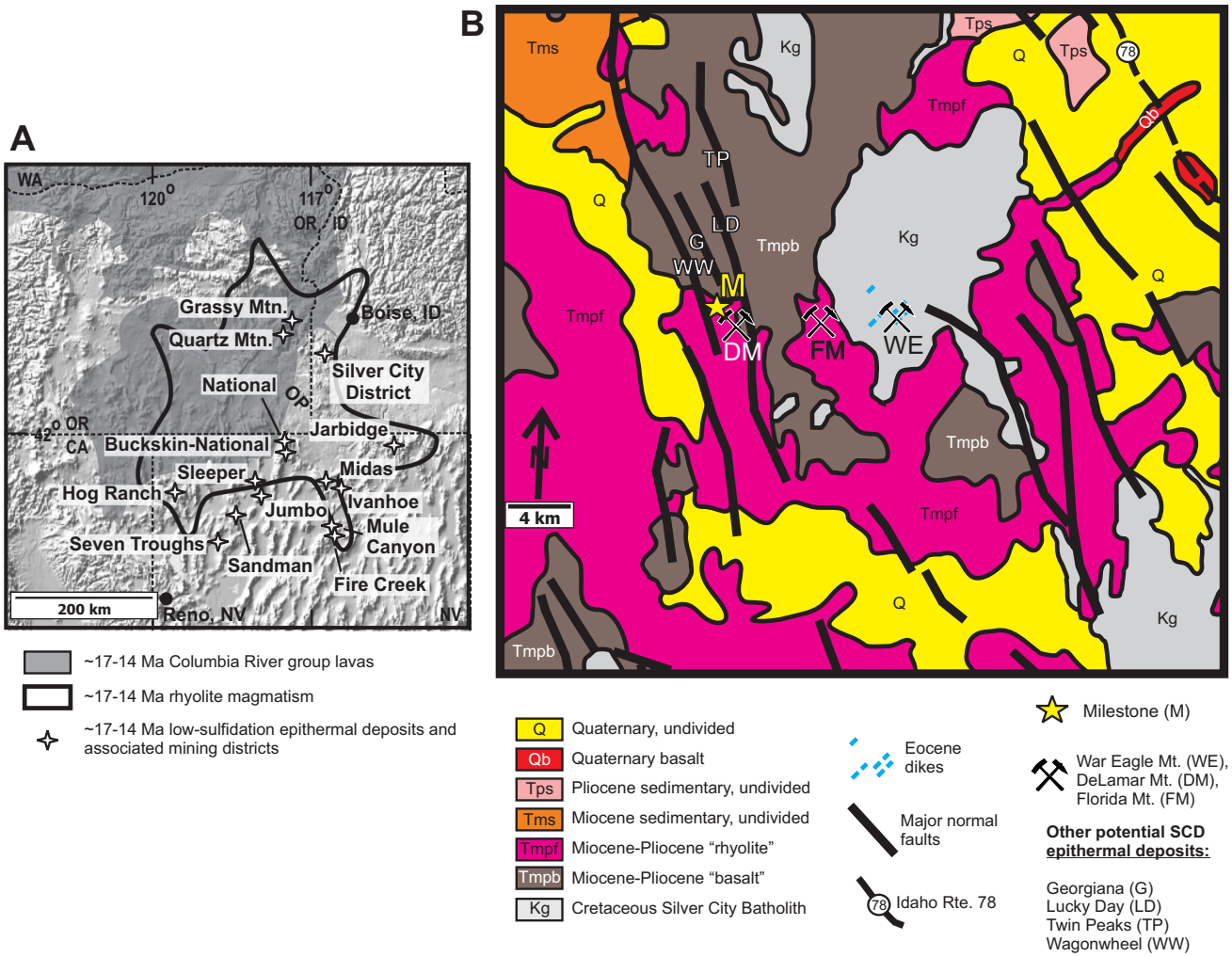

Fig. 1 **A** Map of northern Great Basin (USA) showing ~ 17–14 Ma epithermal Au–Ag deposits/districts, extent of Columbia River Basalt group volcanism, and coeval rhyolite volcanism. Owyhee Mountains study area (Silver City district) is labeled. Abbreviation: OP, Owyhee Plateau. **B** General geological map of Owyhee Mountains, ID (after Ekren et al. 1981; Bonnichsen 1983; Bonnichsen and Godchaux 2006; Mason et al. 2015). Silver City encompasses War Eagle, DeLamar, and Florida mountains. Milestone deposit is marked by yellow "M" along with other deposits Georgiana (G), Lucky Day (LD), and Twin Peaks (TP) along the faults. Wagonwheel sinter lies between Milestone and Georgiana

2001; Kamenov 2007). Considerable debate exists about the role of nano- and microparticles during the process of metal(loid) crystallization, transportation, and deposition in epithermal systems. Detailed textural studies of epithermal ores show that transportation of minerals and metal(loid)s results in the aggregation and deposition of nano- and microparticles by boiling and can form high-grade ore (Saunders 1990; Saunders and Schoenly 1995; Williams-Jones et al. 2009; Saunders et al. 2010; Saunders et al. 2012; Saunders et al. 2019; Zeeck et al. 2021).

Some epithermal Au–Ag deposits were discovered due to the presence of overlying paleohot springs deposits, primarily consisting of siliceous sinter (Sillitoe 2015). Silica sinter deposits are the surficial expression of epithermal ore-forming systems; ~ 300 °C liquids rise through the Earth's crust and boil in the upper kilometer, losing vapor and cooling before discharging at the surface. Amorphous silica, along with other minerals and mineraloids, precipitates from solution upon cooling, forming paleosurface sinter deposits up to tens of meters thick (Fournier 1989; Guido and Campbell 2019; Lynne 2012). Hydrothermal systems transport trace concentrations of metal(loid)s to the surface, where they can be discharged along with the amorphous silica-supersaturated liquid. Thus, silica sinters have the potential to contain various metal(loid)s and represent changes in fluid composition and/or temperature (Vikre 2007).

Paleosurface features, including sinters and hydrothermal breccias, can be used to locate underlying mineral resources (Chang et al. 2011; Lynne 2012; Hamilton et al. 2016). Sinters are exploration indicators for epithermal

Au–Ag veins, but they may be overlooked as economic targets if they are metal-poor (Cunneen and Sillitoe 1989; Sillitoe 2015; J. Hedenquist, pers. communication). Yet, Au concentrations greater than the average upper crustal value (0.0015 ppm; Rudnick and Gao 2003), including many locations with > 1 ppm Au, have been reported from both active and extinct sinters (Weissberg 1969; Fournier et al. 1994; Rice et al. 1995; White et al. 2001; Pope et al. 2005; Hamilton et al. 2016; Campbell et al. 2019; this study). For example, in the Devonian Rhynie Chert (Scotland), up to 0.18 ppm Au has been reported (Rice and Trewin 1988), and Au concentrations up to 85 ppm are associated with As–Sb floc horizons in sinter from Champagne Pool, New Zealand (Weissberg 1969). Sinters are commonly characterized by multicolored laminations or bands, which may represent changes in fluid composition (e.g., metal[loid]-rich vs. metal[loid]-poor), yet the elemental composition of these bands has seldom been studied or quantified (Groves 2007).

Sinters also provide constraints on extreme environments suitable for life, and deposits that preserve high (~ 100 °C) to low (< 35 °C) temperature depositional environments are uncommon (Campbell et al. 2019). Features commonly found in preserved paleosurfaces include bedded sinter (locally recrystallized to chalcedony), irregular/lenticular cavities (bubble-mat texture), geyserite (specular, nodular, columnar), silicified plant material, and hydrothermal breccia (Lynne 2012; Hamilton et al. 2019). The depositional environments of the best-preserved sinters are distinguished based on their proximity to the hot spring vent (Campbell et al. 2019; Hamilton et al. 2019). Deposit temperatures associated with these different facies range from ~ 100 °C at the vent, to the distal and marsh-type facies, as low as ambient temperature (Sillitoe 2015; Hamilton et al. 2019). These different facies have distinctive textures, and studies of active sinters demonstrate that paleohot spring sinters have the same characteristics (e.g., Belhadi et al. 2002; Lynne 2012; Sillitoe 2015).

Geological background

In the SCD and surrounding region, pre-19 Ma magmatic activity was dominated by Cretaceous to Oligocene volcanism related to Farallon plate subduction (Norman and Leeman 1989). At ~ 17 Ma, regional volcanism became primarily compositionally bimodal (Fig. 1), with the eruption of flood basalts (e.g., Columbia River Basalt Group; Steens Basalt in the Oregon Plateau study area) and coeval rhyolite centers (Camp and Ross 2004; Brueseke et al. 2007) related to the Yellowstone hotspot. This phase of magmatism lasted for ~ 3 myr and also coincided both spatially and temporally with extensional tectonism and high-grade low-sulfidation epithermal Au–Ag mineralization in locations across the northern Great Basin including National, Midas, Sleeper, Buckskin-National, and DeLamar (Saunders et al. 2008; Brueseke 2010; Fig. 1).

The SCD was a mid-Miocene eruptive center, characterized by locally erupted Steens flood basalt lavas, andesite-dacite lavas, rhyolite lavas, rhyolite tuffs, and abundant domes/eruptive loci (Halsor et al. 1988; Hasten et al. 2012). These Miocene volcanic rocks overlie older Tertiary to Triassic volcanic rocks, granitoid, and metasedimentary strata (Gillerman et al. 2021). The SCD hosts at least three significant Miocene Au–Ag-rich low-sulfidation epithermal systems (e.g., War Eagle, DeLamar, Florida mts.), which have been historically mined, plus numerous other smaller epithermal systems that are locally associated with broadly coeval rhyolite domes and normal fault zones (Bonnichsen 1983). Most mineralization in the SCD is vein-hosted; however, porous Miocene rhyolite lava also hosts Au–Ag ore. Lead isotope studies of SCD ores (Mason et al. 2015) suggest that the ores were derived from spatially and temporally associated mafic magmas, thus reflecting a mantle origin for the metal(loid)s in SCD deposits like in other northern Great Basin Miocene epithermal ores (Kamenov et al. 2007; Saunders et al. 2015).

The Milestone silica sinter occurrence is located 3 km northwest of the DeLamar deposit (Fig. 1; Electronic Supplementary Fig. 1) and formed on the upper surface of an ~ 16.1 Ma Miocene porphyritic rhyolite lava that hosts high-grade Au and Ag mineralization (Barrett 1985). There is an underlying mineralized matrix-supported hydrothermal breccia (Fig. 2) that lies directly on the rhyolite lava surface (Barrett 1985; Hasten 2012). Milestone formed along a northwest trending normal fault zone that focused rhyolite eruptions, rhyolite dome emplacement, fluid flow, and epithermal mineralization and associated alteration (Fig. 1; Barrett 1985; Halsor et al. 1988; Hasten et al. 2012; Gillerman et al. 2021). Most of the mineralization along this fault zone (e.g., Lucky Day, Twin Peaks, Georgiana prospects; locally named the Black Sheep district) occurs in veins based on reconnaissance exploration drilling (Gustin et al. 2019); other mapped sinter terraces in this zone are extensive, over several square kilometers (Gillerman et al. 2021).

The paleosurface at Milestone is characterized by a mineralized breccia and overlying layered sinter (Figs. 2, 3, 4, 5, and 6). As mentioned, Lindgren (1900) was the first to briefly describe the Milestone sinter deposit (hereafter named the "Main Knob"), consisting of "flinty grayish to brown quartz with numerous organic remains [and] undeterminable grasses." Reconnaissance assays of bulk sinter samples returned grades of up to 7.09 g/t (ppm) Ag and 2.83 g/t Au (Barrett 1985). For comparison, bulk-rock assays from SCD veins and rhyolite-hosted breccia and stockwork ore range up to ~ 200 g/t Au and 30,000 g/t Ag (Mason et al. 2015).

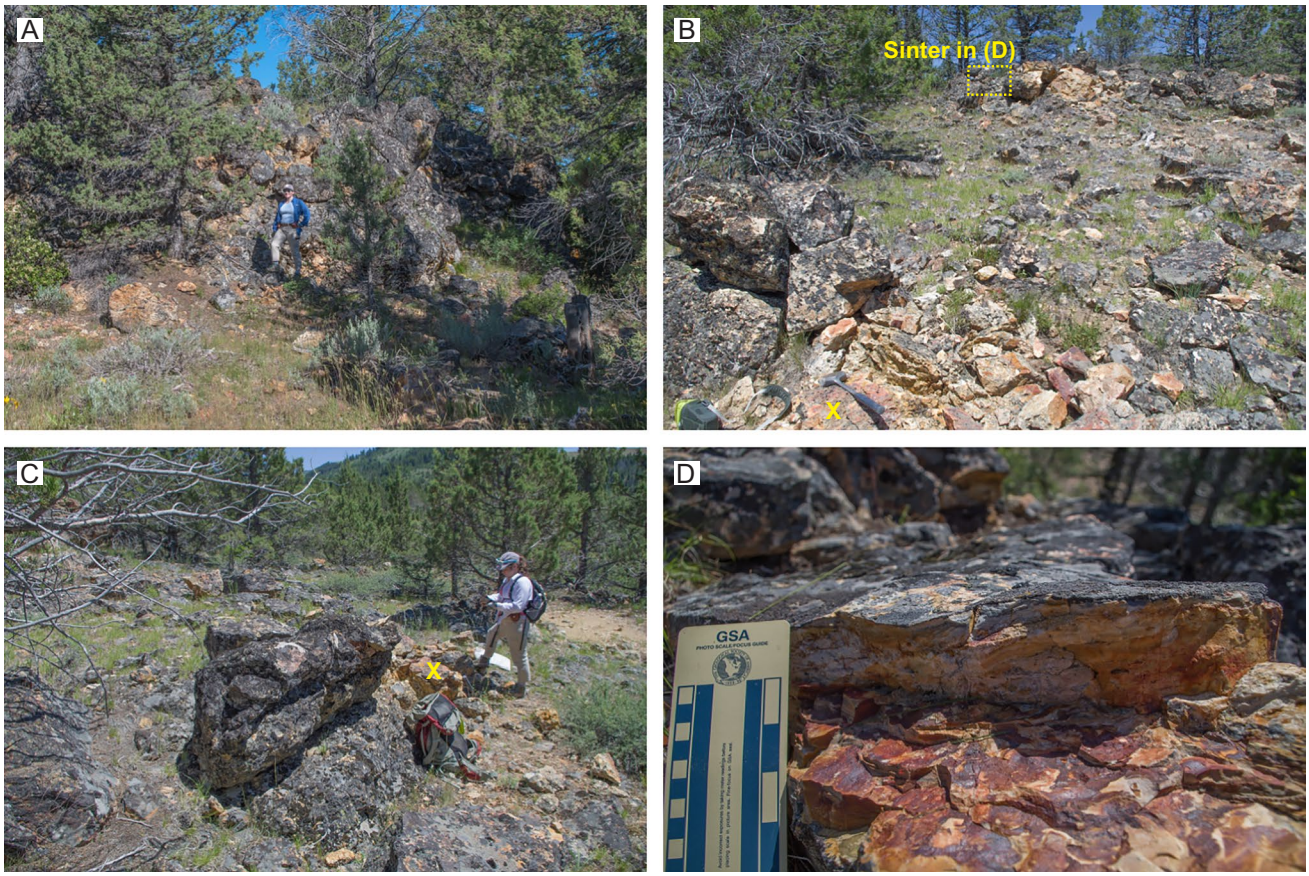

Fig. 2 Field photos of the Main Knob at Milestone. **A** View of the Main Knob outcrop from mining road. Person for scale. **B** View from the bottom of the Main Knob pointed up-slope. Rock marked with yellow "X" is matrix-supported breccia in **C** marked with same yellow "X." **C** Matrix-supported breccia at the bottom of the Main Knob. **D** Broken banded sinter resulting in a relatively flat surface covered in oxidation staining and lichen

Barrett (1985) sketched Milestone deposit and surrounding bedrock and created cross-sections of the geology and subsurface alteration from core logs in an effort to provide more detail on the geological setting and mineralogy of the deposit. The Milestone sinter is layered amorphous silica characterized by massive, laminated textures. Cross-cutting metal-poor veins and silica gel injections host colloform, comb, pseudo-acicular quartz, chalcedony, and lattice-bladed quartz-after-calcite pseudomorphs; the entire sinter deposit is characterized by minor hydrothermal alteration that postdated sinter deposition (Barrett 1985; our mapping). Ore minerals in the sinters include pyrargyrite (Ag_3SbS_3), naumannite (Ag_2Se), electrum, and tetrahedrite ($Cu_9Fe_3Sb_4S_{13}$), whereas gangue includes quartz, pyrite, illite, montmorillonite, kaolinite, marcasite, and jarosite (Barrett 1985).

Methods

Our mapping focused on the sinter and breccia facies and deposit stratigraphy, as well as collecting samples for geochemical and mineralogical study. Sample locations were determined based on geological mapping (Barrett 1985; this study) and our field observations. The observations made at the Main Knob were used to create a detailed geologic map of the site (Fig. 3). Different sinter and breccia types on the Main Knob were grouped into five main lithofacies: banded sinter, massive plant-rich sinter, and geyserite sinter (along with notable features such as bubble mat and stromatolite bioformations), plus matrix-supported and clast-supported fragmental deposits. Sampling criteria for the sinter included defined bedding laminations, suitable for point and line analysis by laser ablation inductively coupled plasma mass spectrometry

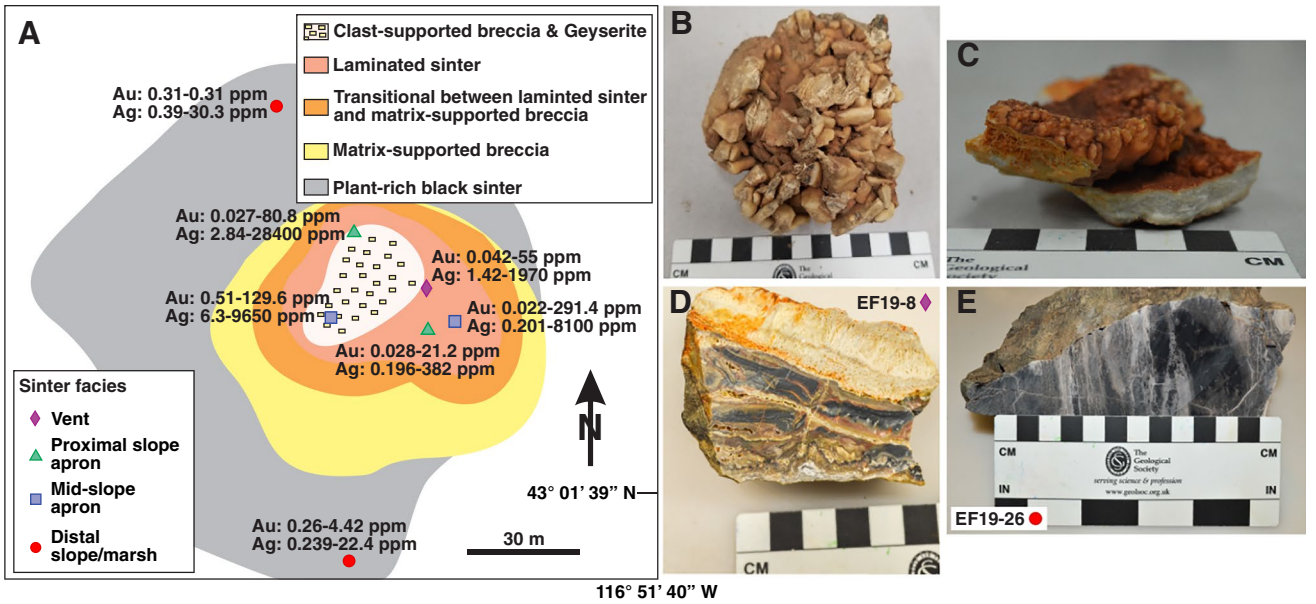

Fig. 3 **A** Sketch of the Milestone Main Knob, with sinter facies and sample locations with measured ranges of Au and Ag concentrations. **B** Clast-supported breccia (vent facies) with clasts cemented together by a chalcedony coating. **C** Nodular geyserite. **D** Metal(loid)-rich banded white to dark gray banded sinter, also with quartz after calcite pseudomorphs (uppermost lamination). **E** Metal(loid)-poor massive black sinter (distal facies)

(LA-ICP-MS). Sinter that lacked consistent bedding was noted and also sampled for its fossil content, distance from vent location, and/or hydrothermal textures. Matrix-supported breccias have textures indicating gradation and fluvial action and locally are interbedded with sinter; clast-supported breccias have variable clast size around the site. Adjacent to the Main Knob, samples were collected based on color, bedding, and plant fossil content to help identify the furthest extent of preserved paleosurface. Another sinter deposit, located ~ 3 km north-northwest of Milestone known as Wagonwheel (Fig. 1B), was sampled for comparison.

A total of 26 samples were collected from the Milestone Main Knob and surrounding area, including Wagonwheel. Fourteen 30-micron-thick thin sections and twelve doubly polished 150-micron-thick sections (for laser ablation analysis) were cut from sinter samples. All thin sections were described using reflected light microscopy. Imaging was performed using a Zeiss Axioscope reflective light microscope attached with a Zeiss Axiocam.

Quantitative and spatial relationships of trace metal(loid)s were investigated using LA-ICP-MS. We examined laminated sinter (e.g., white, tan, dark-gray, black, pink red, brown-colored), with LA-ICP-MS trace element analyses acquired using a New Wave Research/ESI 193-nm excimer laser ablation system coupled to a Thermo Scientific iCapQ quadrupole mass spectrometer housed at the Trace Element and Radiogenic Isotope Lab (TRaIL) at the University of Arkansas. Six slabs and five polished double-thick sections were analyzed by transects perpendicular to sinter bands or transects that crossed the most bands. Four of the remaining polished thick sections were chosen for spot analyses (transect and spot data are reported here and all results are in Electronic Supplementary Materials [ESM] File 1). Ablation spots along transects were spaced at 350 µm. Each analysis utilized a 100-µm laser spot, a repetition rate of 10 Hz with a burst of 200 shots, and a fluence of ~ 9.5 J/cm^2. In total, 26 masses were analyzed: ^{29}Si, ^{32}S, ^{23}Na, ^{27}Al, ^{39} K, ^{48}Ti, ^{57}Fe, ^{197}Au, ^{107}Ag, ^{63}Cu, ^{66}Zn, ^{75}As, ^{111}Cd, ^{118}Sn, ^{121}Sb, ^{77}Se, ^{125}Te, ^{202}Hg, ^{205}Tl, ^{73}Ge, ^{208}Pb, ^{195}Pt, ^{105}Pd, ^{209}Bi, ^{232}Th, and ^{238}U. Ge was only analyzed for in the slab transects, and Pt and Pd were only analyzed for in the spot analyses. All elements were detected in analyzed samples. NIST standard glass 612 (Jochum et. al 2011) was used as the primary standard with NIST610 glass as a secondary standard. Data reduction was performed using the Iolite Software (Paton et al. 2011). ^{29}Si (99% for unknowns) was used for standardization. The RSD for all elements were < 5% except for S whose RSD was ~ 8%. Si, S, Se, Te, and Hg are reported in counts per second (cps) as there was no standard for these elements, every other element is reported in parts per million (ppm). Possible minor interferences for Se include Ar, K, and Ca, but are generally < 10 ppb. Se concentrations mimic Au, Ag, and Te; thus, we interpret any possible interference to be low.

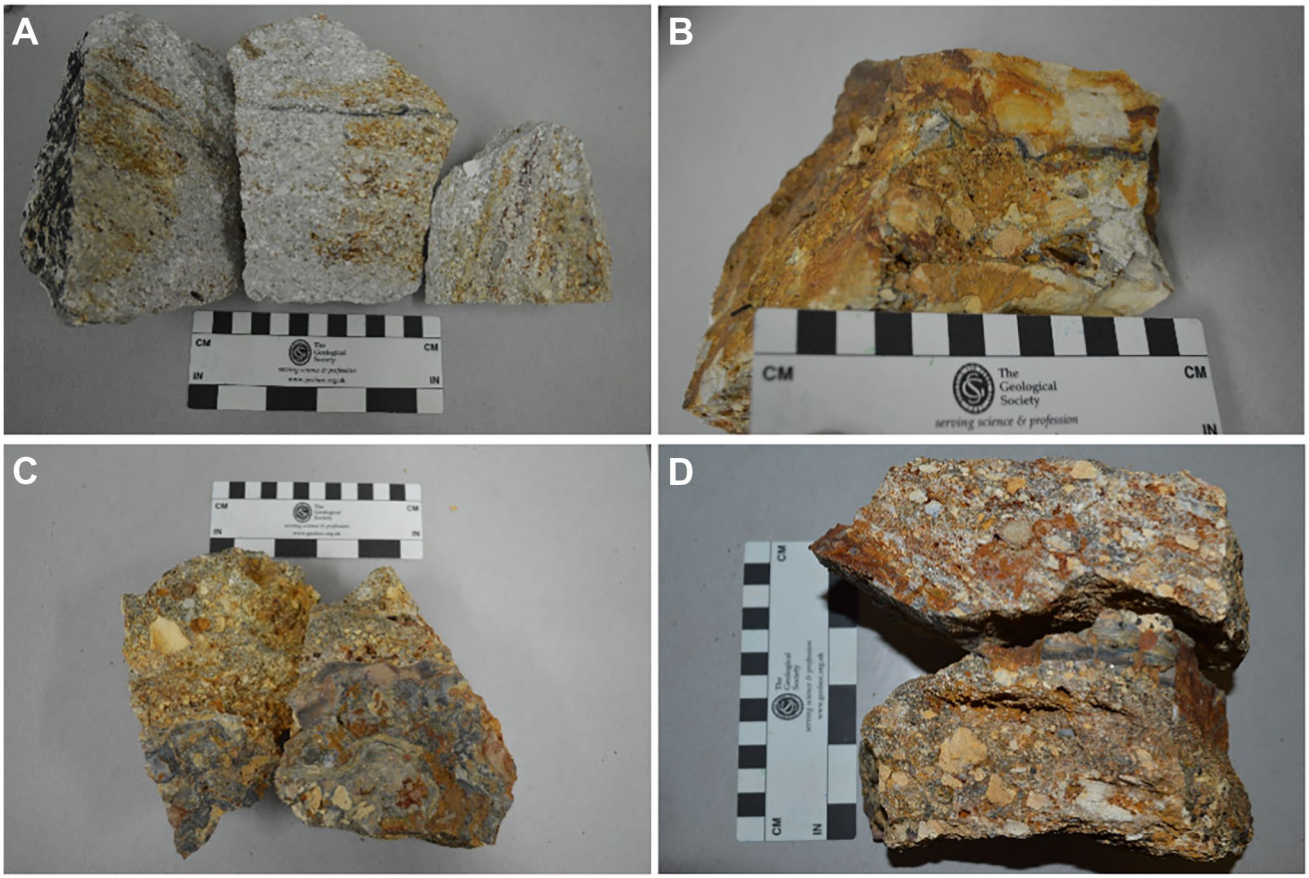

Fig. 4 Matrix-supported breccia. Unsorted grain sizes range from ~ 0.1 to 8 cm. Matrix consists of white, gray, tan, or black sinter, with fine (~ 0.3 cm) interbedded layers of banded sinter. **A** Matrix supported breccia consisting of gray-colored sinter matrix with white altered rhyolite clasts (up to ~ 2 cm) and a single layer of interbedded black sinter. **B** Light-tan matrix-supported breccia with an oxidized surface containing large clasts (~ 8 cm) of altered rhyolite. **C** Matrix-supported breccia with overlying dark-gray/black sinter. **D** Gray matrix-supported breccia with unsorted clasts and interbedded black sinter overlying the breccia

Results

Our mapping and field description of the Milestone Main Knob demonstrate that sinter and breccia from the deposit represent five lithofacies: (1) sinter, including multi-colored laminated sinter and massive gray-black sinter with plant remains; (2) geyserite; (3) bubble mat (e.g., microbiological dominated features, including stromatolites and wavy laminated sinter with bubble mat features); (4) clast-supported breccia, cross-cut by near-vent silica gel; and (5) matrix-supported breccia.

The areal extent of the Main Knob is ~ 0.8 km^2, with much of the deposit exposed at the surface. The spatial relationships of mappable units on the Main Knob (Fig. 3) include two types of breccia: matrix-supported (Fig. 4) and clast-supported (Fig. 5). The clast-supported breccia occurs in the center of the deposit, whereas the matrix-supported breccia is more common on the edges (Fig. 3). The clast-size of the clast-supported breccia ranges from ~ 2.5 to 10 cm (Fig. 6), whereas the matrix-supported breccia varies from fine pebbles (~ 0.1 cm) up to large boulders that might be ballistics (12 cm) (Fig. 4). The clast size increases with distance from the deduced vent location. The clast-supported breccia is only present on the northeastern side of the knob, surrounded by the sinter on all sides (Fig. 3).

Banded sinter is located in the center of the knob and extends beyond the clast-supported breccia; massive black sinter (Fig. 6) occurs on the outer flanks of the deposit site. Abundant plant fossils, including twigs and small logs, are common across the center of the knob in both the sinter and matrix-supported breccia (Fig. 6). Geyserite sinter covers most of the central area of outcrop, adjacent to the clast-supported breccia, and occurs as nodular, spicular, ripple, and pisoids (Fig. 7), features that indicate the locations of hot springs vents. Microbial accumulations such as bubble mat and spherical stromatolites (Fig. 8) were limited to a large boulder of sinter on the southeastern side of the Main Knob.

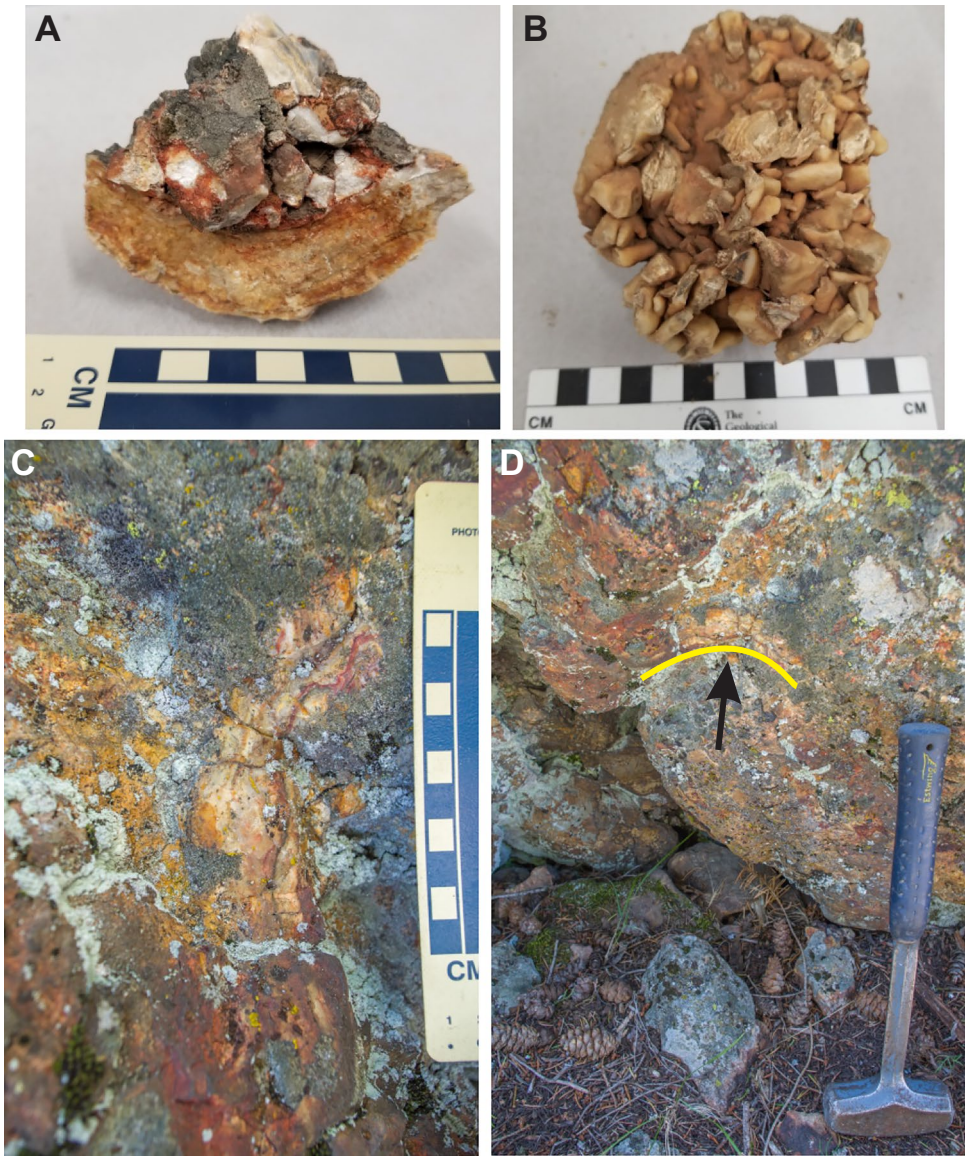

Fig. 5 Rock samples of clast-supported breccia and silica gel. **A** Portion of clast-supported breccia that deposited onto a sinter horizon, thus deforming it upon impact. **B** Clast-supported breccia with varying clast sizes cemented together by a final coating of sinter. **C**, **D** Silica gel (highlighted by yellow line and arrow) along pre-existing cracks in the underlying host rock. Image C is rotated 90° from horizontal

Lithofacies

Matrix-supported breccia

Description The breccia clasts are primarily unsorted, clay-altered Silver City rhyolite that are rounded. Clast sizes range from small pebbles (< ~ 0.1 cm) to boulders up to ~ 12 cm in size. The outer portions of some samples are moderately oxidized and other breccia contains a layer of injected black sinter (Fig. 4). The matrix consists of a whitish tan to a light/dark gray sinter. Thin layers of sinter (~ 2 mm thickness) are interbedded in the breccia, but these bands are sparse. All samples have both rounded to angular clasts. However, matrix-supported breccias with predominantly gray sinter tend to have a higher abundance of rounded clasts (~ 80% of clasts) than those with tan, black, or white sinter (~ 60–70% of clasts). All clasts are pervasively altered sinter or rhyolite.

Interpretation This lithofacies formed from the result of hydrothermal eruption (Hedenquist and Henley 1985; Hamilton et al. 2019). The sinter matrix and lateral extent of this facies (~ 75 m × 90 m) suggest a high-volume eruption. The rhyolite and existing sinter were incorporated in the eruption. The high population of rounded clasts indicates milling in the conduit and eruption column, entraining more angular clasts in the process. The angular clasts in the tan, white, or black matrix-supported breccias indicates an early period of eruption while the milled clasts reflect lower eruption velocities and less explosiveness (Hedenquist and Henley 1985; Tămaş and Milési 2003).

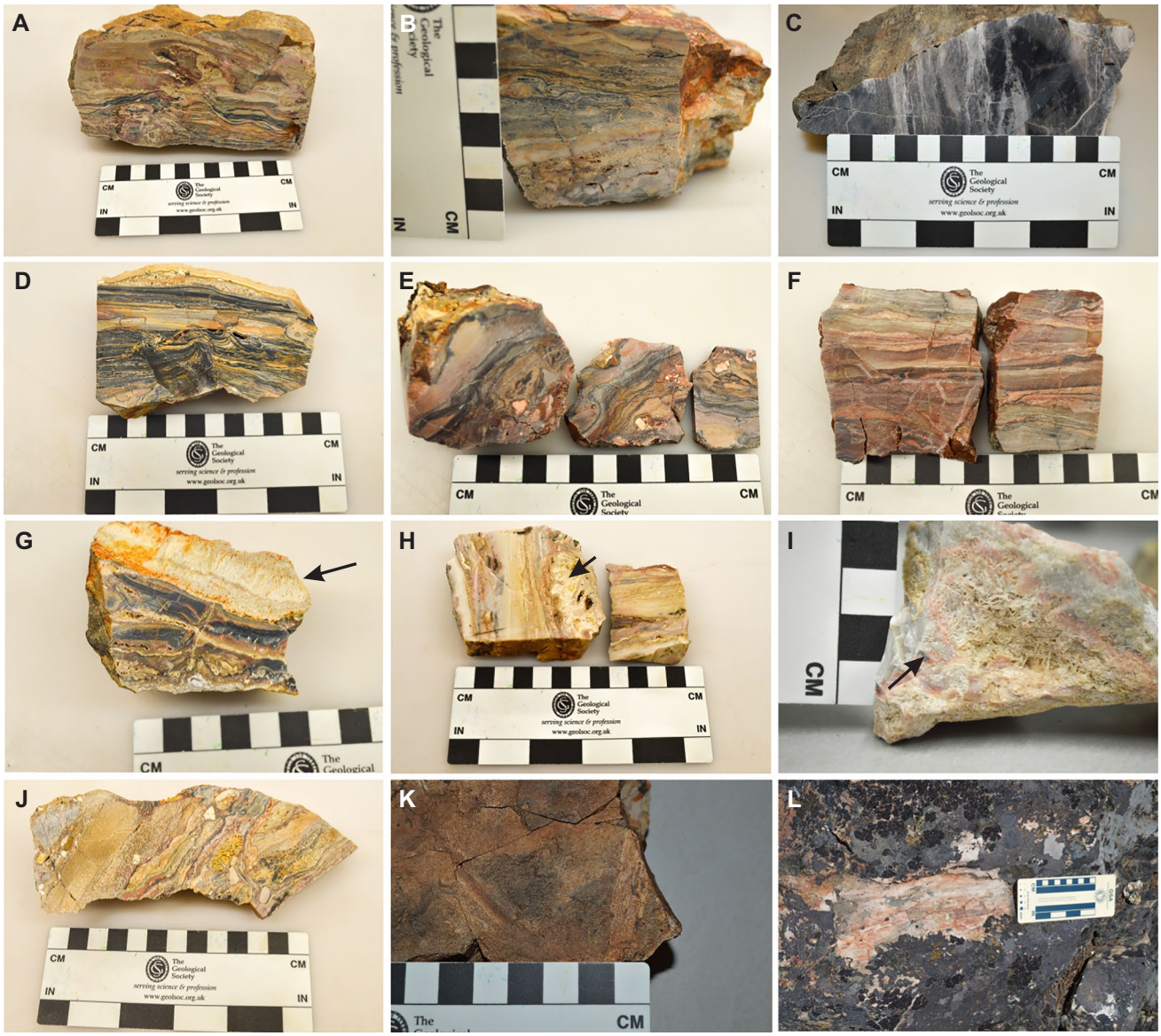

Fig. 6 Samples of colorful banded sinter. **A** Beds of sinter deformed by fluid injection while existing as a silica gel. **B** Banded sinter interbedded with sediments. **C** Massive black sinter with irregular light gray bedding. **D** Defined silica bedding with slight deformation, fracturing, and interbedded sediments. **E** Irregular sinter layers deformed by and interbedded with angular sinter clasts. **F** Defined silica bedding oxidized from Fe content. **G–I** Slightly deformed layers between sinter beds incorporating sinter clasts and quartz after calcite pseudomorphs (highlighted by arrows). **J** Transitional sinter layering dominated by interbedding of sinter and hydrothermally altered rhyolite clasts. **K**, **L** Wood fragments ranging from small twigs to medium-sized logs

Clast-supported breccia

Description Angular sinter and clay-altered rhyolite clasts are more uniform in size compared to the matrix-supported breccia. Clast size ranges from very coarse sand to small cobbles (Fig. 5A, B), and the clasts are loosely to moderately packed. Individual clasts are coated by a thin (~ 1–2 mm) layer of amorphous silica with little to no matrix, leaving open space between clasts (Fig. 5A, B). Fallout of this breccia is present on a bed of curved sinter, forming bomb sags (Fig. 5A). Silica gel is also present and becomes more common with depth (Fig. 5C, D). Amorphous silica gel is present in hot springs near the surface where it forms via vapor loss during boiling (e.g., well-documented in the 1989 Porkchop geyser eruption in Yellowstone; Fournier et al. 1991). It can be injected into the overlying geyser mound and sinter pile (e.g., sinter infiltrate of Campbell et al. 2019) and is also a fundamental component of epithermal veins (Saunders 1990). In Milestone, silica gel is composed of primarily white and tan amorphous silica that fills in the

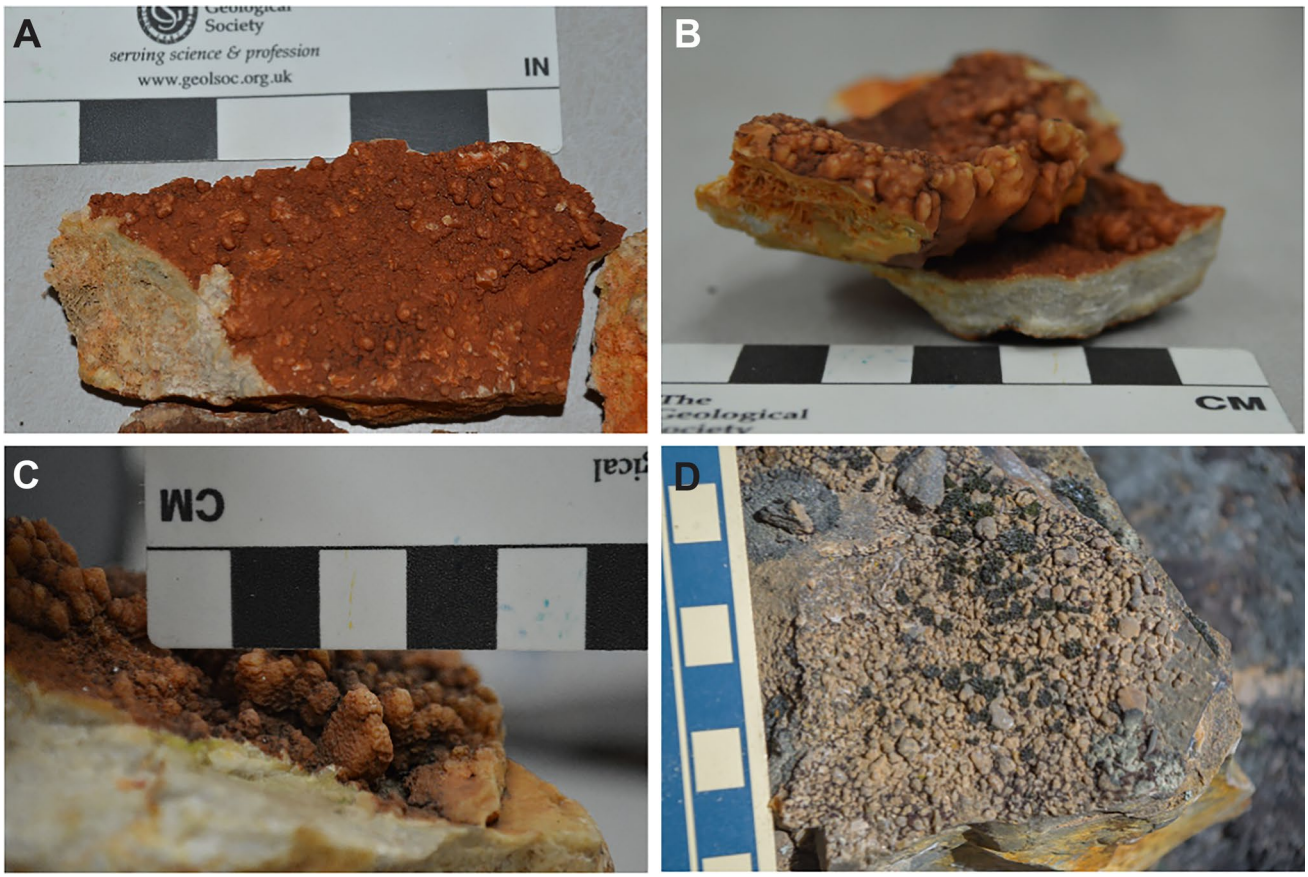

Fig. 7 Geyserite from the Main Knob of Milestone. **A**, **B** Botryoidal geyserite covering quartz after calcite textures. **C** Nodular geyserite of column-like pillars or stalagmites. **D** Geyserite pisoids cemented by amorphous silica

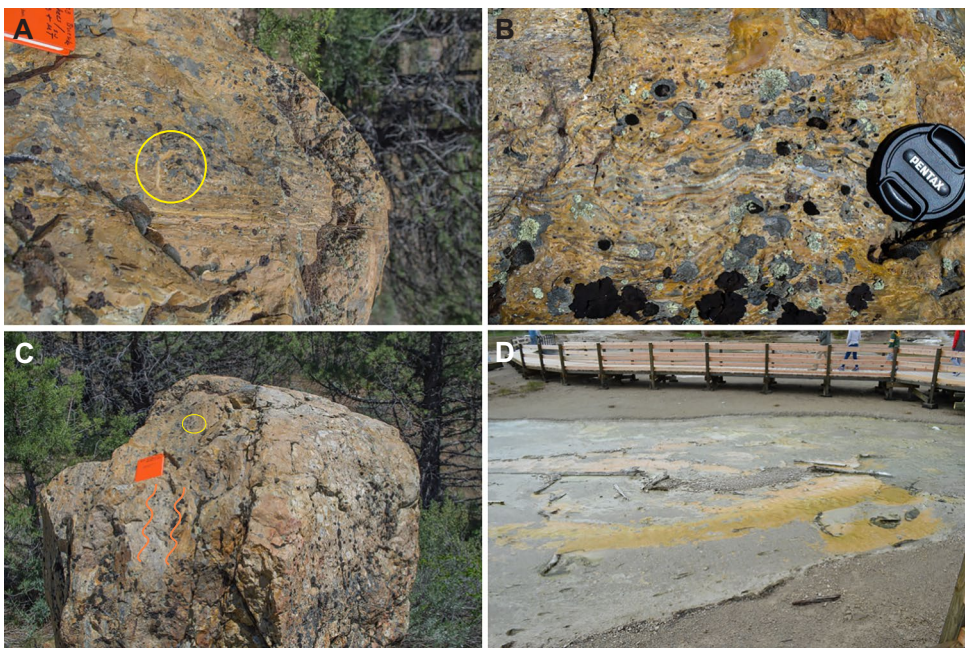

Fig. 8 Microbial features at Milestone. **A** Cross section of stromatolites (yellow circle) growing on and with sinter beds. **B** Low-amplitude wavy sinter laminations encompassing flattened, oval-like gas bubbles. **C** Boulder that shows sinter with microbial textures (yellow circle). **D** Microbial mat thermophilic algae growing in the outflow discharge of Porcelain Basin at Yellowstone, Wyoming

open spaces between clasts of the clast-supported breccia, cracks in the country rock, and between sinter beds. Silica gel is more localized in the clast-supported breccia on the northeast side of the Main Knob. Wood clasts are preserved in this facies and include smaller branches to twigs.

Interpretation The angular clasts and lack of matrix, plus the limited areal extent of this deposit (~ 20 m × 30 m), are consistent with a vent conduit. This likely formed via a hydrothermal eruption. This discharge coated the breccia clasts with amorphous silica to cement the clasts together. The sinter bed with impact features that some portions of this breccia rest upon suggests that the newest sinter in the area was not yet hardened and still existed as a silica gel at the time of vent collapse. The curved sinter bed that some portions of this breccia rest upon suggests that the newest sinter in the area was not yet hardened and still existed as a silica gel at the time of vent collapse. Silica gel is fed through shallow hydrothermal feeders that are positioned immediately under geyser vents; thus, the presence of the gel in this context (e.g., sinter infiltrate) is consistent with a vent (Campbell et al. 2019). The silica gel most commonly fills in open spaces of the clast-supported breccia and nearby country rock at depths of about 1 m below the current topographic surface (Fig. 5C, D).

Sinter

Description Multi-colored banded sinter beds form the proximal apron over the Main Knob. Individual beds are ~ 1 mm thick and envelop epiclastic deposits in some areas. Sinter colors include white, tan, dark-gray, black, red, and brownish (Fig. 6). Some zones between sinter beds also contain quartz-after-calcite (QAC) textures and vary in size (Fig. 6G–J). Fossils of small twigs to logs also occur within this facies (Figs. 6K, L).

Interpretation The variation of color in the sinter samples may be due to changes in the composition in the hot spring discharge. In several samples, the original horizontal bedding was disturbed through an influx of liquid (Fig. 6A, D, G). Thin beds (> 1 cm) of sediment between sinter beds are interpreted to be the result of changing drainage paths over the surface, smaller eruptions of material, and varying discharge flow rates (Fig. 6B, D, G, J). The QAC textures are evidence of boiling liquids that postdate sinter formation.

Geyserite

Description Nodular geyserite forms small (~ 3 mm high) stalagmite-like features along with botryoidal geyserite proximal to the vent and overlying sinter beds (Fig. 7A–C). Rounded pebbles and spheroids (up to ~ 4 mm) of geyserite (e.g., bead-sized pebbles or pisoids; Hamilton et al. 2019) were coated by sinter over the pisoids, cementing them to the surface on which they were deposited (Fig. 7D). An oxidized crust covers the surface of all geyserite samples, which overlies the bedded sinter was exposed to the atmosphere.

Interpretation The geyserite pisoids initially formed in shallow pools in the splash zone around the vent (> ~ 75 °C) and were pushed away by the flow of liquid to be gathered further downslope. As these pisoids are delicate in nature, their preservation suggests that formation occurred after the vent eruption and collapse; their occurrence downslope of the vent suggests that their formation occurred before the formation of the nodular and botryoidal geyserite. The nodular and botryoidal geyserite formed in the splash zone of the discharged liquid.

Bubble mat facies

Description Microbiological textures include wavy laminated sinter, rare warm pool-related stromatolites, and flattened bubbles between sinter beds (Fig. 8A, B). The stromatolite features are evidenced by concentric layers of sinter (Fig. 8A). The most abundant microbial textures were found in an ~ 2 × 2-m boulder located on the drill road surrounding the Main Knob that was disturbed by exploratory drilling at the deposit in the 1980s (Fig. 8C).

Interpretation Concentric features and small, oval-shaped gas bubbles that deformed horizontally bedded sinter may be due to thermophilic microbes in the flanks of the hot spring vents (Fig. 8D). The circular sphere-like formations in the sinter could be stromatolitic. Oxygen gas bubbles respired by these microbes through photosynthesis were trapped and deformed with the sinter beds (Hamilton et. al 2019). Thermophiles such as these can be similar to the microbial mats found around hot springs in Yellowstone National Park, which require ~ 45–55 °C to thrive (Hamilton et. al 2019), thus suggesting that the microbes exist in the distal apron.

Deposit mineralogy

We observed pyrite as both disseminated euhedral crystals and clusters. Clusters include cubic and octahedral crystals up to ~ 3 µm in size. Larger crystals (about 100 µm in size) are also present. The relict grains and sinter beds with finely disseminated to no visible pyrite are partially oxidized to hematite. Pyrargyrite was identified in only one sample, where it occurs as an anhedral crystal ~ 1 mm in size, amongst jigsaw quartz.

Electrum microparticles are present predominantly within the dark gray/black layers of Milestone sinter (Figs. 6 and 9). The disseminated grains occur as either small globules

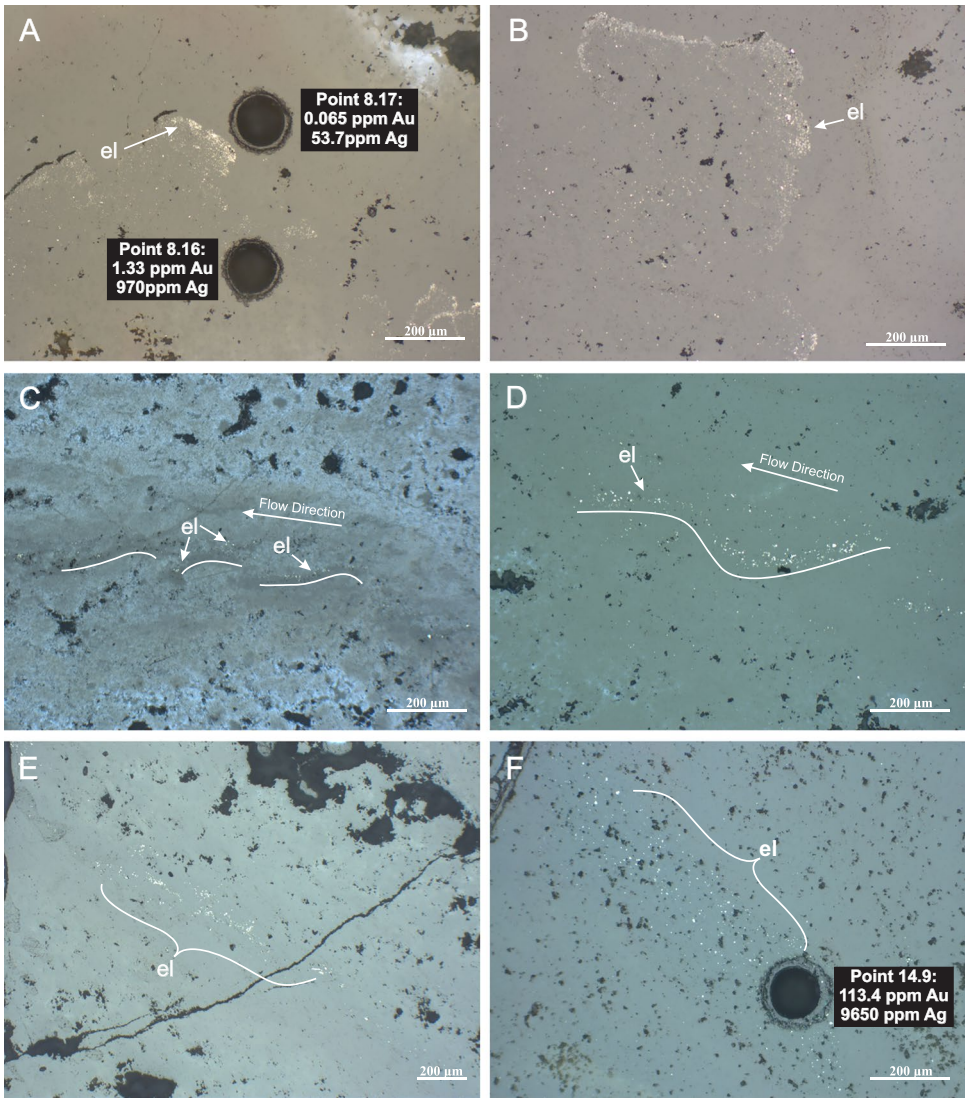

Fig. 9 Reflected light (RFL) photomicrographs of electrum. **A**, **B** Dendritic crystals of electrum enveloped by amorphous silica with electrum on the leeward side of sinter ripples. **C** Chalcedony and **D** the same chalcedony, in a different location showcasing microparticles of sluice-box textured electrum. Fluid flow is from right to left. **E**, **F** Disseminated electrum microparticles in sinter beds

or as flecks up to 30 µm in size (Fig. 9). Where visible, these grains can appear disseminated or as an accumulation, overlying a former silica gel surface. We interpret the structures in Fig. 9C, D to be sinter ripples (Campbell et al. 2015), where metal(loid) microparticles accumulate on the side of sinter ripples (Fig. 9C, D). This may be analogous to nano- and microparticle accumulation on the leeward side of protrusions and ripples in epithermal veins, creating a sluice-box texture (Saunders et al. 2010; Saunders 2012). At Milestone, the particles are slightly more disseminated to patchy in the sinter directly beneath ripples (Fig. 9A, B), consistent with cross sections through electrum dendrites (Saunders et al. 2010; Saunders 2012; Saunders and Burke 2017).

Quartz is the primary and most abundant gangue mineral in the Milestone Main Knob deposit and occurs with different textures. The sinter itself is layered amorphous silica that locally contains jigsaw quartz. Jigsaw quartz is the most common texture after amorphous sinter. Jigsaw quartz may be a recrystallization texture of chalcedony, opaline silica, or silica gel that requires a temperature of ~ 180 °C to form (Fournier 1989; Saunders 1994; Moncada et al. 2012). In thin section, this texture contains fine anhedral quartz grains that are, on average, less than 3 µm up to ~ 5 µm in size. Cross-cutting veins host chalcedony, colloform, comb, and pseudo-acicular quartz.

In Milestone, quartz-after-calcite textures appear as lattice-bladed, interspersed within sinter layers. The blades have overgrowths of comb quartz growing towards the center of the void space. In epithermal veins, bladed calcite replaced by silica is common and forms via boiling, followed by replacement via silica-bearing liquid (Simmons and Christenson 1994). We interpret these textures to reflect late-stage boiling liquid in the host sinter, after burial; this is consistent with cross-cutting relations in the sinter.

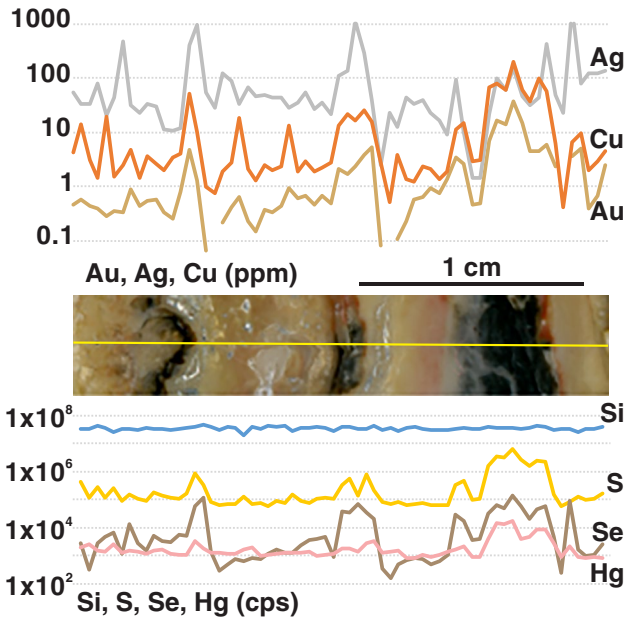

Fig. 10 Representative LA-ICP-MS transect (yellow line) of vent sample EF19-8 (middle) and data for representative metal(loid)s in ppm (above) and cps (below). The dark-colored sinter bands are enriched in metal(loid)s and sulfur, relative to tan-pink bands, with little change in silicon concentrations

Sinter composition

Trace element concentrations vary widely and between sinter bands (Fig. 3). LA-ICP-MS transects and point analyses confirm the presence of Au and Ag in the black and dark gray bands of the sinter (Figs. 6, 9, and 10; ESM 1, 2, 3). In all sinters, white, light gray, and light tan laminae have the lowest concentrations of all measured elements; samples that consist of predominantly red sinter contain elevated concentrations of Fe and Hg by at least one order of magnitude (ESM 2, 3). The plant-rich black sinter that represents distal depositional facies has the lowest ranges of concentrations of Au and Ag, at < 5 ppm and 30 ppm, respectively (Fig. 3). Overall, Au concentrations range from 0.03 to 291 ppm, whereas Ag varies to a larger extent (0.19–28,400 ppm) in analyzed sinters. Spots and transects that cut across clasts show elevated concentrations of Si, Al, and K, confirming the entrainment of clasts of the underlying rhyolite (ESM 1, 2).

Despite the variation of the measured elements, there does not appear to be a clear correlation between element concentrations (Au, Ag, Cu, Se, Te, Hg) and distance from the vent over the ~ 200 m we mapped and sampled (Figs. 3 and 11). Figure 11 illustrates this relationship as a function of Au, Ag, and Se concentrations. Some facies, such as the mid-slope apron, had many samples, thereby providing a wider range of chemical data, whereas only one sample from the vent was analyzed. Collectively, the sinter bands in the vent sample show a narrower range of elemental concentrations. Generally, the highest Au and Ag concentrations are associated with higher Se concentrations, as well as other elements such as Hg, Te, As, and S (Fenner 2020). This may be due to the presence of microparticles of selenium and mercury minerals such as naumannite (Ag_2Se), cinnabar (HgS), As-rich pyrite, and other Au–Ag–Se–S phases, all reported in sinters from the northern Great Basin (Vikre 2007). The highest Ag concentrations are present in proximal slope apron sinter (EF19-6), whereas the highest Au concentrations are in mid-slope apron sinter (Fig. 11). The highest Au value (291 ppm) also contains 1291 ppm Ag, which is low compared to the highest Ag concentration (28,400 ppm) in the sinter.

Discussion

Milestone paleosurface formation

Geologic mapping indicates that the massive black sinter is the oldest exposed portion (e.g., stratigraphically lowest; Fig. 3) of the Milestone deposit. This extends as far as 480 m from the vent to the southeast (not depicted on Fig. 3), deposited in local topographic lows that existed across a rhyolite lava–dominated paleosurface (Fig. 3). The black sinter contains silicified plants.

The next phase of the system was hydrothermal eruptions that deposited material as far as ~ 50 m from the vent and formed the matrix-supported breccia. As this phase ceased, more fluids were discharged to create facies of interbedded clast-dominant and fluid-dominant beds; subsequently, silica-rich fluids were discharged from the vent to form the bedded sinter. Based on the overall thickness of the sinter facies, this was the second longest phase recorded in the hydrothermal system. This phase had sufficient flow rates (Walter et al. 1996; Hamilton et al. 2018) to form thermophilic algae and related bubble mats and stromatolites, similar to that in the Porcelain Basin of Yellowstone (Fig. 12). A later hydrothermal eruption formed the clast-supported breccia, which broke up the vent conduit and caused its collapse. Renewed silica discharge and sinter deposition within the collapsed vent conduit occurred, and geyserite also deposited at the surface during this phase. Geyserite pisoids formed at the base of the vent, followed by a coating of sinter. Nodular and specular geyserite were also deposited proximal to the vent. All features at the Main Knob are noted with relation to each facies and where they may lie on a schematic diagram for sinter paleosurface features (Fig. 13; Hamilton et al. 2019).

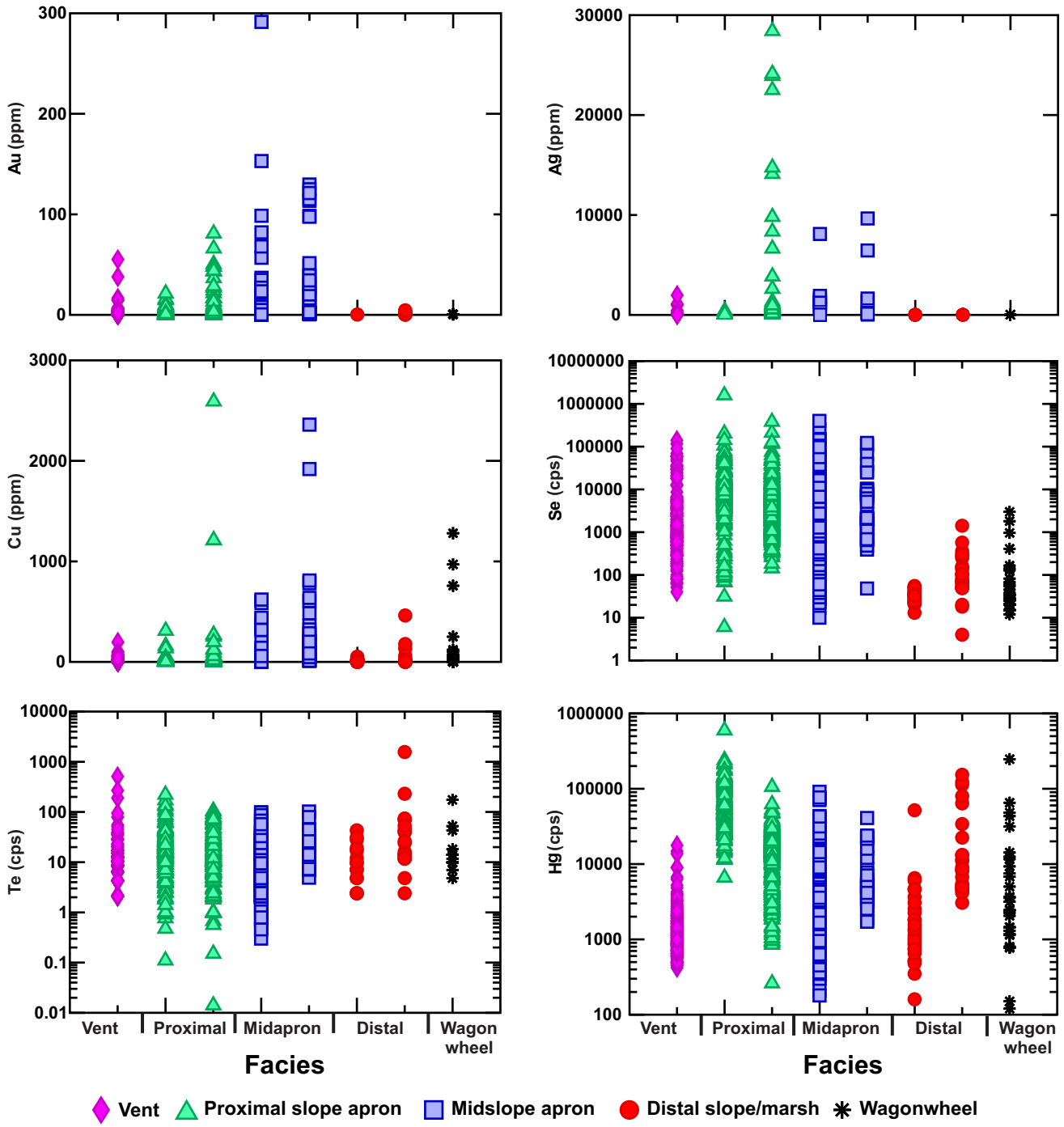

Fig. 11 Concentrations of metal(loid)s as a function of sinter facies. As distance from the vent increases (to the right), temperature decreases. Concentrations are either in parts per million (ppm; Au, Ag, Cu) or expressed as counts per second (cps; Se, Te, Hg)

Implications of Milestone sinter compositions

Visible occurrences of metal-bearing minerals (e.g., electrum) in the Milestone deposit occur in the bedded sinter, rather than in cross-cutting veins. The concentrations of Au, Ag, and Cu across the Main Knob are 0.027–291 ppm, 0.19–28,400 ppm, and 0.11–2590 ppm, respectively. Overall, the highest concentrations of metal(loid)s, particularly Au and Ag (up to 291 ppm and 28,400 ppm, respectively), occur in the black and gray layers of the banded sinter, < 30 m from the inferred vent (Fig. 3). Milestone sinter Au and Ag values overlap with reported bulk rock Au concentrations from high-grade SCD veins (Mason 2015).

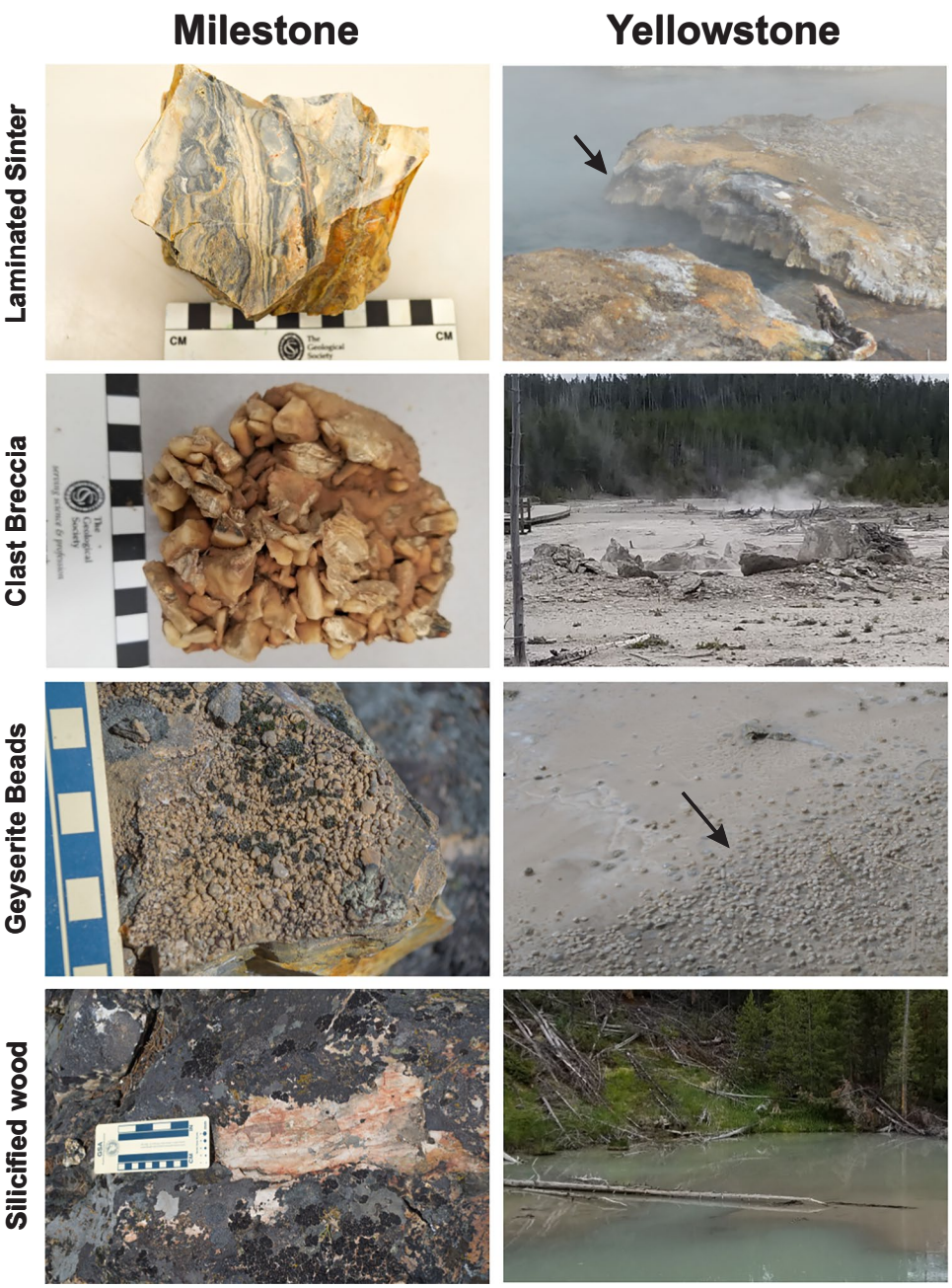

Fig. 12 Comparison of hot spring features between Milestone (left) and Yellowstone (right). From top to bottom: laminated sinter from the Main Knob and at Beryl Spring, clast-supported breccia from the Main Knob and at Porcelain Basin, geyserite pisoids from the Main Knob and at Porcelain Basin, and silicified wood from the Main Knob and at Porcelain Basin

We interpret the sluice-box textures of electrum in Milestone samples to have formed via surface flow of water discharged from the hot spring vent. This is in contrast to fluid flow that formed Au–Ag-rich veins documented by Saunders et al. (2010) and Saunders (2012), where the sluice-box nano- and microparticle textures formed below the surface during fluid ascent in epithermal veins. At Milestone, occurrences of Au–Ag–Se minerals in syngenetic sinter deposits formed by flowing solutions from the paleohot spring, rather than in veins created by a late-phase injection of fluid. The textural evidence we present indicates that metal(loid) nano- and microparticles existed prior to their deposition in the sinter (Saunders et al. 2010, 2019; Saunders 2012; Moncada et al. 2012; Saunders and Burke 2017). Similar sized microparticles were identified in coeval epithermal veins by Saunders et al. (2019) and were concluded to have grown from smaller electrum nanoparticles. We attribute the variable elemental concentrations between individual sinter beds to discharge of metal-rich and metal-poor fluids, analogous to banded colloform and crustiform zones of metal-rich and metal-poor bands in some epithermal veins (e.g., dark gray to black, high-grade Au and Ag-rich ginguro bands; Tharalson et al. 2019). Thus, the dark, metal(loid)-rich sinter beds may reflect metal(loid) pulses into the geothermal fluid,

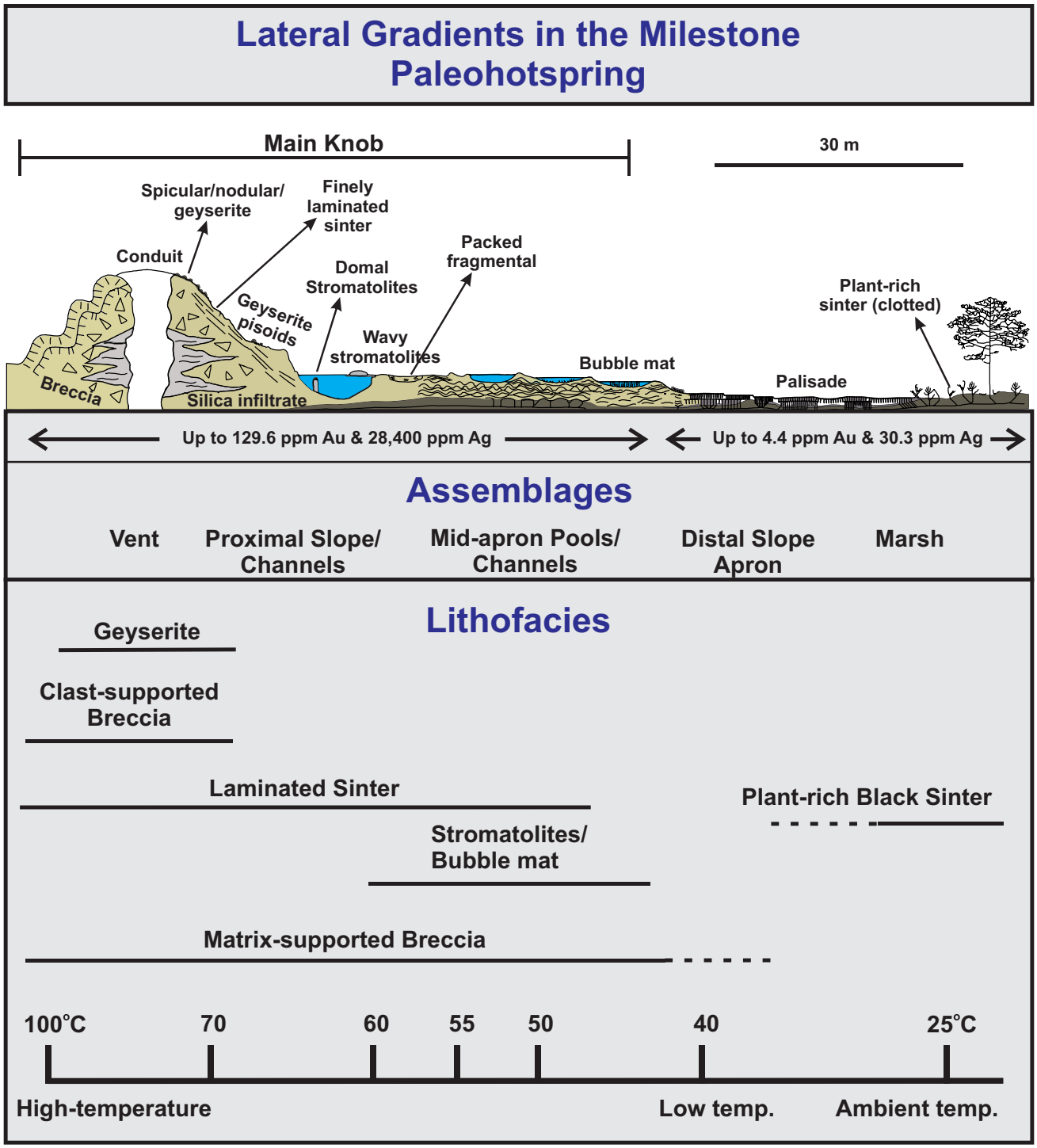

Fig. 13 Paleosurface cartoon for Milestone. The surface features are aligned with their geographic assemblages, the lithofacies defined in this study, and possible temperature of formation.Modified from Hamilton et al. (2019)

followed by surface discharge. Pope et al. (2005) speculated that transportation of native gold nanoparticles may be a mechanism for Au transfer away from the Champagne Pool vent, to downstream portions of the sinter, analogous to what we document in the Milestone sinter. In epithermal systems like Milestone, precious and base metals, if not already present as nanoparticles in the ascending hydrothermal fluid, commonly precipitate closer to the vent and grade outwards to lower concentrations in distal parts of the sinter (Sillitoe 2015; Hamilton et al. 2016; Clark and Gemmell 2018). An

example of this is the Kohuamuri sinter in New Zealand, where high to low concentration of elements from vent to marsh aided in the identification of ore at depth (Hamilton et al. 2016). The concentrations of Au and Ag as a function of location across the Main Knob (Fig. 11) indicate that there are no observable pattern relating to the geometry and facies-based sinter. The temperature of surface liquid discharge did not control the formation of Milestone metal(loid) particles. We suggest that the nano- and microparticles were transported from a deeper source to the surface and entrained across the Main Knob, consistent with the sluicebox textures we observe in the sinter.

Mid-Miocene northern Great Basin hot springs systems and active analogues

Milestone crops out just northwest of the DeLamar mine, where epithermal mineralization has been mined for over a century. Mineralization at Milestone is present in the banded dark-colored beds of sinter (this study) and in the matrix-supported breccia (Barrett 1985). Economic minerals at DeLamar, and also at nearby Florida Mountain, are hosted in veins, mineralized breccias, and porous rhyolitic units (Lindgren 1900; Bonnichsen 1983; Mason 2015; Gustin et al. 2019). Major north northwest-trending faults northwest of DeLamar were pathways at Milestone, Lucky Days, Twin Peaks, Georgiana, and Wagonwheel (Fig. 1). Halsor et al. (1983) suggested that the local rhyolite domes were emplaced along preexisting faults and Milestone sinter deposition soon followed. Barrett (1985) also reported the hot spring forming after the faulting and rhyolite volcanism, consistent with rhyolite clasts in the Milestone breccias and the sinter deposit overlying Silver City Rhyolite. These rhyolite lavas, dated at 16.1 Ma by $^{40}Ar/^{40}Ar$ on sanidine (Brueseke and Hames, unpublished data), underlie the Milestone sinter. Adularia from epithermal veins from Florida Mountain and War Eagle Mountain has been dated at ~ 15.5–15.8 Ma (Aseto 2012; Mason et al. 2015), which cut the rhyolite package; thus, it is likely that the hydrothermal system that formed Milestone was related to this same postrhyolite mineralization event that affected the entire SCD.

Milestone facies reflect a paleohot spring setting, with facies that include sinter, bioformations, geyserite, silicified plant material (including large pieces of wood intermingled with the eruption breccia), and eruption breccias. What we document at Milestone is similar to present-day hot spring system and also to previously studied mid-Miocene epithermal paleosurfaces in the northern Great Basin. For example, the Ivanhoe, Midas, and Buckskin-National deposits are other mid-Miocene epithermal systems in the northern Great Basin that share a similar geologic history with the SCD. In all of these locations, local Mid-Miocene magmatism was controlled by coeval extensional faulting (John et al. 2003; Wallace 2003; Vikre 2007; Brueseke and Hart 2008; Brueseke 2010). Mercury-Au mineralization at Ivanhoe was coeval with local rhyolite domes that erupted along extensional fault zones in the area (Wallace 2003). The hydrothermal fluids associated with mineralization migrated to the surface along these faults and clay-altered rhyolite lavas and tuffs. At Ivanhoe, the mercury deposits are in the sinter, and the Au lies within the underlying tuffs and subsurface vein deposits (Wallace 2003). At its paleosurface, the sinter deposits at Ivanhoe contain surface vents, outflow breccias, parallel bedding, and massive sinter, similar to Milestone. At Midas, mid-Miocene mafic dikes and sills, as well as sedimentary deposits crop out in proximity to extensional faults. Locally, hot spring vents, sinter, and silicified breccias are also aligned with the local faults (Leavitt et al. 2004). At Buckskin-National, mercury-rich sinter has been reported in a small basin surrounded by rhyolite lavas and domes, and intercalated with volcaniclastic sediments and tuffs (Vikre 2007), adjacent to an active extensional basin and multi-vent volcanic field (Brueseke and Hart 2008; Brueseke 2010). There, metal(loid) zonation in underlying epithermal veins has been directly linked to coupled textural-geochemical metal(loid) zonation and layering in the sinter (Vikre 2007); this relationship is also likely present at Milestone.

It is also useful to compare Milestone to active hot springs environments, such as those in Yellowstone National Park and the Taupo Volcanic Zone in New Zealand. In Yellowstone, normal faults are related to regional extension and ring fractures adjacent to the Yellowstone caldera (Fournier 1989; Morgan et al. 2017). Local hydrothermal activity is especially pronounced in these fault zones (Fournier 1989). Silica sinters occur in several areas in the park, but primarily in these normal fault zones, as hot spring pools, mounds, and terraces. Yellowstone contains numerous hot springs with all the same features found at Milestone (e.g., bioformations, sinter, clast-supported breccia, and geyserite) (Fig. 12). Furthermore, Beryl Spring contains up to ~ 1.6 ppm Au in its sinter (Fournier et al. 1994). The Taupo Volcanic Zone hosts relatively young (< 340 ka) mineralized epithermal systems in a part of New Zealand that is undergoing rifting (Barker 1993; Rowland and Simmons 2015). There, rift-related faults act as a series of structurally controlled pathways for ascending fluids. The Au–Ag mineralization and clay alteration in the Taupo Volcanic Zone is associated with the structural weaknesses and fault-aligned eruptive centers in the rift basins, much like the SCD has rhyolite domes and mineralized areas, including Milestone, localized on the normal faults in the Owyhee Mountains. In New Zealand, the hot-spring vents produce surface features similar to those found on the Main Knob, such as eruption breccia, plant-rich fabrics, domal stromatolites, and wavy banded sinter (Drake et al. 2014).

Conclusions

1. Five lithofacies are present in the Milestone deposit at Main Knob: plant-rich black massive sinter, banded sinter beds, geyserite, clast-supported breccia, and hydrothermal matrix-supported. These lithofacies record proximal (hotter) to distal (cooler) parts of the surface discharge of a neutral pH hydrothermal system, with the system punctuated by hydrothermal eruptions. The Milestone deposit also hosts bioformations, including stromatolites, which indicate sustained discharge and high flow rates. We have identified one of the hydrothermal vents from which discharge (and eruptions) was sourced. These paleosurface features are analogous to those in active hydrothermal systems (e.g., Yellowstone), as well as other northern Great Basin Miocene systems characterized by coeval normal faulting and volcanism.
2. Milestone banded sinter varies in color from tan and/or pink to dark gray/black. The black layers contain the highest concentration of trace metal(loid)s, including up to 291 ppm Au and 28,400 ppm Ag, bound primarily in sulfides, selenides, and electrum. The identification of the hot spring vent and metal(loid)-rich sinters suggest that precious metal-rich veins exist at depth below the Milestone deposit.
3. At the Milestone Main Knob, there is no observable pattern of trace metal(loid)s content with increasing distance from the mapped paleohot spring vent, based on our analyses of sinter layers and spot analyses. This observation suggests that the temperature of fluids at the surface did not play a substantial role in the formation of electrum and other ore-bearing minerals in proximal deposits. Rather, these minerals were likely transported to the surface as nano- and microparticles and entrained in the flow across the sinter, as evidenced by the sluicebox textures and dendritic aggregates.

Supplementary Information The online version contains supplementary material available at https://doi.org/10.1007/s00126-022-01117-z.

Acknowledgements Supporting analytical data and figures can be found in online Supplemental Files. This research was part of Fenner's M.Sc. thesis at Kansas State University and was made possible in part by funding from the Geological Society of America (Fenner), Society of Economic Geologists (Fenner), and the American Federation of Mineralogical Societies (Fenner and Brueseke). We acknowledge Integra Resources Corp. for field support and an internship to Fenner in summer 2019. We thank Aryton Hamilton, Jeff Hedenquist, Jim Saunders, Richard Sillitoe, and an anonymous reviewer plus Associate Editor Hartwig Frimmel and Editor-in-Chief Georges Beaudoin for their constructive feedback on various versions of this manuscript.

Declarations

Funding Geological Society of America,Society of Economic Geologists,American Federation of Mineralogical Societies

Conflict of interest The authors declare no competing interests.

References

Aseto CO (2012) Geology, geochemistry, and geochronology of low-sulfidation epithermal Au-Ag ores on War eagle Mountain, Silver City District, Idaho. M.S. thesis, Auburn University

Barker R (1993) The history of epithermal gold-silver exploration in the Taupo Volcanic Zone. New Zealand Mining 12:15–19

Barrett R (1985) The geology, mineralization, and geochemistry of the milestone hot-spring silver-gold deposit near the Delamar silver mine, Owyhee county, Idaho. M.S. thesis, University of Idaho

Belhadi A, Nakanishi T, Watanabe K, Izawa E (2002) Gold mineralization and occurrence of sinter in the Hoshino area, Fukuoka Prefecture, Japan. Resour Geol 52:371–380

Bonnichsen B, Godchaux MM (2006) Geologic map of the Murphy 30 x 60 quadrangle, Ada, Canyon, Elmore, and Owyhee Counties, Idaho: Idaho Geological Survey DWM-80

Bonnichsen B (1983) Epithermal gold and silver deposits Silver City-De Lamar district, Idaho: Idaho Geological Survey Technical Report 83–4, 29 pp

Brueseke ME, Heizler MT, Hart WK, Mertzman SK (2007) Distribution of Oregon Plateau (U.S.A.) flood basalt volcanism: the Steens Basalts revisited. J Volcanol Geoth Res 161:187–214

Brueseke M, Hart WK (2008) Geology and petrology of the mid-Miocene Santa Rosa-Calico volcanic field, northern Nevada: Nevada Bureau of Mines and Geology, Bulletin 113

Brueseke ME (2010) Magmatism and mineralization in the Oregon Plateau and northern Great Basin: mid-Miocene volcanism and associated bonanza ore deposits and their relations to the inception of the Yellowstone hotspot. In: Steininger R, Pennell WM (eds) Proceedings of the Geological Society of Nevada Symposium, Great Basin Evolut Metal, Reno-Sparks, pp 247–254

Butterman WC, Amey EB III (2005) Mineral commodity profiles – gold, United States Geological Survey Open-File Report 02–303, 66 pp

Campbell KA, Guido DM, Gautret P, Foucher F, Ramboz C, Westall F (2015) Geyserite in hot-spring siliceous sinter: window on Earth's hottest terrestrial (paleo)environment and its extreme life. Earth Sci Rev 148:44–64

Campbell KA, Guido DM, Vikre JDA, Rhys PG, D and Hamilton, A, (2019) The Miocene Atastra Creek sinter (Bodie Hills volcanic field, California and Nevada): 4D evolution of a geomorphically intact siliceous hot spring deposit. J Volcanol Geoth Res 370:65–81. https://doi.org/10.1016/j.jvolgeores.2018.12.006

Camp VE, Ross ME (2004) Mantle dynamics and genesis of mafic magmatism in the intermontane pacific northwest. J Geophys Res 109. https://doi.org/10.1029/2003JB002838

Chang Z, Hedenquist JW, White NC, Cooke DR, Roach M, Deyell CL, Garcia J Jr, Gemmell JB, McKnight S, Cuison AL (2011) Exploration tools for linked porphyry and epithermal deposits: example from the Mankayan intrusion-centered Cu-Au district, Luzon, Philippines. Econ Geol 106:1365–1398

Clark LV, Gemmell JB (2018) Vein stratigraphy, mineralogy, and metal zonation of the Kencana low-sulfidation epithermal Au-Ag deposit, Gosowong Goldfield, Halmahera island, Indonesia. Econ Geol 113:209–236. https://doi.org/10.5382/econgeo.2018.4549

Cunneen R, Sillitoe RH (1989) Paleozoic hot spring sinter in the Drummond basin. Queensland, Australia: Economic Geology 84:135–142

Drake BD, Campbell KA, Rowland JV, Guido DM, Browne PRL, Rae A (2014) Evolution of a dynamic paleo-hydrothermal system at Mangatete, Taupo Volcanic Zone, New Zealand. J Volcanol Geoth Res 282:19–35. https://doi.org/10.1016/j.jvolgeores.2014.06.010

Ekren EB, McIntyre DH, Bennett EH, Malde HE (1981) Geologic map of Owyhee County, Idaho, west of longitude 116°W. U.S. Geol Survey, Map 1–1256

Ekren EB, McIntyre DH, Bennett EH, Marvin RF (1982) Cenozoic stratigraphy of western Owyhee County, Idaho, *in* Bonnichsen, B. and Breckenridge, R.M., eds., Cenozoic Geology of Idaho, Idaho Bureau of Mines and Geology Bulletin 26

Fenner ER (2020) Paragenesis and geochemistry of the Miocene Milestone sinter, Silver City District, ID: implications for sinter-hosted epithermal Au-Ag deposits. MS thesis, Kansas State University

Fournier RO (1989) Geochemistry and dynamics of the Yellowstone National Park hydrothermal system. Annual Review of Earth Sciences: U.S. Geological Survey 17:13–53

Fournier RO, Thompson JM, Cunnigham CG, Hutchinson RA (1991) Conditions leading to a recent small hydrothermal explosion at Yellowstone National Park. Geology 103:1114–1120

Fournier RO, Kennedy B, Mack AM, Thompson JM (1994) Correlation of gold in siliceous sinters with $^{3}He/^{4}He$ in hot spring waters of Yellowstone National Park. Geochim Cosmochim Acta 58:5401–5419

Gillerman VS, Feeney, DM, Canada, AS, Schmidt, KL (2021) Geologic map of the De Lamar and Swisher Mountain quadrangles, Owyhee County, Idaho. Idaho Geol Survey Digital Web Map 193. https://www.idahogeology.org/product/DWM-193

Groves SR (2007) The geology and genesis of the Moonlight Prospect, Pajingo Epithermal System, Northland Queensland: an investigation of a high-level, low sulfidation epithermal system. MS Thesis, University of Tasmania

Guido DM, Campbell KA (2019) Plastic silica conglomerate with an extremophile microbial matrix in a hot-water stream paleoenvironment. Astrobiology 19:1433–1441. https://doi.org/10.1089/ast.2018.1998

Gustin MM, Weiss SI, McPartland JS (2019) Technical report and updated resource estimate for the Delamar and Florida Mountain gold-silver project, Owyhee County, Idaho. Mine Development Associates, Integra Resources Corp, USA

Halsor S (1983) A volcanic dome complex and DeLamar silver mine, Owyhee County, Idaho. M.S. thesis, Michigan Technological University

Halsor SP, Bornhorst TJ, Beebe M, Richardson K, Strowd W (1988) Geology of the DeLamar silver mine, Idaho – a volcanic dome complex and associated hydrothermal system. Econ Geol 83:1159–1169

Hamilton A, Campbell K, Rowland J, Browne P (2016) The Kohuamuri siliceous sinter as a vector for epithermal mineralization, Coromandel Volcanic Zone, New Zealand. Miner Deposita 52:181–196. https://doi.org/10.1007/s00126-016-0658-8

Hamilton AR, Campbell KA, Guido DM (2019) Atlas of siliceous hot spring deposits (sinter) and other silicified surface manifestations in epithermal environments. GNS Sci 56, https://doi.org/10.21420/BQDR-XQ16

Hames W, Unger D, Saunders J, Kamenov G (2009) Early Yellowstone hotspot magmatism and gold metallogeny. J Volcanol Geoth Res 188:214–224

Hasten Z (2012) Mid-Miocene magmatism in the Owyhee Mountains, ID: origin and petrogenesis of volcanic rocks in the Silver City District. M.S, thesis, Kansas State University

Hasten Z, Brueseke M, Saunders J, Hames W (2012) Mid-Miocene volcanism in the Owyhee Mountains (ID) and implications for coeval epithermal precious metal mineralization Geochimica et Cosmochimica Acta, Goldschmidt Conference Abstracts, 2012

Hedenquist JW, Henley RW (1985) Hydrothermal eruptions in the Waiotapu geothermal system, New Zealand: their origin, associated breccias, and relation to precious metal mineralization. Econ Geol 10:1640–1668

Heinrich CA, Audétat GD, Ulrich A, T, Frischknecht R, (1999) Metal fractionation between magmatic brine and vapor, determined by microanalysis of fluid inclusions. Geology 27:755–758

Jochum KP, Wilson SA, Abouchami W, Amini M, Chmeleff J, Eisenhauer A, Hegner E, Iaccheri LM, Kieffer B, Krause J, McDonough WF (2011) GSD-1G and MPI-DING reference glasses for in situ and bulk isotopic determination. Geostand Geoanal Res 35:193–226. https://doi.org/10.1111/j.1751-908X.2010.00114.x

John DA (2001) Miocene and early Pliocene epithermal gold-silver deposit in the Northern Great Basin, western United States: characteristics, distribution, and relationship to magmatism. Econ Geol 96:1827–1853

John DA, Hofstra AH, Fleck RJ, Brummer JE, Saderholm EC (2003) Geologic setting and genesis of the Mule Canyon low-sulfidation epithermal gold-silver deposit, north-central Nevada. Econ Geol 98:425–463

Jones B, Renaut RW, Rosen MR (2001) Biogenicity of gold- and silver-bearing siliceous sinters forming in hot (75°C) anaerobic spring-waters of Champagne Pool, Waiotapu, North Island, New Zealand. J Geol Soc 158:895–911

Kamenov GD, Saunders JA, Hames WE. Unger DL (2007) Mafic magmas as sources for gold in middle Miocene epithermal deposits of the Northern Great Basin, United States: evidence from Pb isotope compositions of native gold. Econ Geol 102:1191–1195, 0361–0128/07/3696/5/5–1191

Leavitt ED, Spell TL, Goldstrand PM, Arehart GB (2004) Geochronology of the Midas low-sulfidation epithermal gold-silver deposit, Elko County, Nevada. Economic Geology 99:1665–1686, 0361–0128/01/3475/1665–22

Lindgren W (1900) The gold and silver veins of the Silver City, De Lamar, and other mining districts in Idaho. U.S. Geological Survey 20th Annual Report. Part 3:65–256

Lindgren W (1933) Mineral Deposits. McGraw-Hill Book Company, New York

Liu YS, Hu ZC, Li M, Gao S (2013) Applications of LA-ICP-MS in the elemental analyses of geological samples. Chinese Science Bulletin, Geochemistry 58:3863–3878. https://doi.org/10.1007/s11434-013-5901-4

Lynne BY (2012) Mapping vent to distal-apron hot spring paleo-flow pathways using siliceous sinter architecture. Geothermics 43:3–24

Moncada D, Mutchler S, Nieto A, Reynolds TJ, Rimstidt JD, Bodnar RJ (2012) Mineral textures and fluid inclusion petrography of the epithermal Au-Ag deposits at Guanajuato, Mexico: Application to exploration. J Geochem Explor 114:20–35

Morgan LA, Shanks WCP, Lowenstern JB, Farrell JM, Robinson JE (2017) Geologic field-trip guide to the volcanic and hydrothermal landscape of the Yellowstone Plateau, U.S. Geol Survey Scie Investigations Rep 2017–5022–P, 100, https://doi.org/10.3133/sir20175022P

Norman MD, Leeman WP (1989) Geochemical evolution of Cenozoic-Cretaceous magmatism and its relation to tectonic setting, southwestern Idaho, U.S.A. Earth Planet Sci Lett 94:78–96

Paton C, Hellstrom J, Paul B, Woodhead J, Hergt J (2011) Iolite: freeware for the visualisation and processing of mass spectrometric data. J Anal at Spectrom 26:2508–2518. https://doi.org/10.1039/C1JA10172B

Pope JG, Brown KL, McConchie DM (2005) Gold concentrations in springs at Waiotapu, New Zealand: implications for precious metal deposition in geothermal systems. Econ Geol 100:677–687

Rice CM, Trewin NH (1988) A Lower Devonian gold-bearing hot-spring system, Rhynie, Scotland. Transactions of the Institution of Mining and Metallurgy Section B Applied Earth Science 97:141–144

Rice CM, Ashcroft WA, Batten DJ, Boyce AJ, Caulfield JBD, Fallick AE, Hole MJ, Jones E, Pearson MJ, Rogers G, Saxton JM, Stuart FM, Trewin NH, Turner G (1995) A Devonian auriferous hot spring system, Rhynie, Scotland. J Geol Soc 152:229–250

Williams-Jones AE, Bowell RJ, Migdisov AA (2009) Gold in solution. Elements 5:281–287

Rudnick RL, Gao S (2003) The composition of the continental crust. In: Holland HD, Turekian KK (eds) Treatise on Geochemistry, Vol. 3, The Crust, Elsevier-Pergamon, Oxford, pp 1–64. http://dx.doi.org/10.1016/b0-08-043751-6/03016-4

Saunders JA (1990) Collodial transport of gold and silica in epithermal precious metal systems: evidence form the Sleeper deposit, Humboldt County, Nevada. Geology 18:757–760

Saunders JA (1994) Silica and gold textures in bonanza ores of the Sleeper Deposit, Humboldt County, Nevada: evidence for colloids and implications for epithermal ore-forming processes. Econ Geol 89:628–638

Saunders JA (2012) Textural Evidence of Episodic Introduction of Metallic Nanoparticles into Bonanza Epithermal Ores: Minerals 2:228–243

Saunders JA, Schoenly PA (1995) Boiling, colloid nucleation and aggregation, and the genesis of bonanza Au-Ag ores of the sleeper deposit, Nevada. Miner Deposita 30:199–210

Saunders JA, Burke M (2017) Formation and aggregation of gold (electrum) nanoparticles in epithermal ores: Minerals 7:1–11. https://doi.org/10.3390/min7090163

JA Saunders DL Unger GD Kamenov M Fayek WE Hames WC Utterback 2008 Genesis of middle Miocene Yellowstone hotspot-related bonanza epithermal Au-Ag deposits, Northern Great Basin, USA Miner Deposita 43 https://doi.org/10.1007/s00126-008-0201-7

Saunders JA, Hofstra AH, Goldfarb RJ, Reed MH 2014 Geochemistry of hydrothermal gold deposits, *in* Holland HD and Turekian KK, eds., Treatise on geochemistry, Second Edition, Elsevier 13 383–424

Saunders JA, Mathur R, Kamenov GD, Shimizu T, Brueseke ME (2015) New isotopic evidence bearing on bonanza (Au-Ag) epithermal ore-forming processes. Miner Deposita 51:1–11. https://doi.org/10.1007/s00126-015-0623-y

Saunders JA, Burke M, Brueseke ME (2019) Scanning-electron-microscope imaging of gold (electrum) nanoparticles in middle Miocene bonanza epithermal ores from northern Nevada, USA. Miner Deposita 55:389–398. https://doi.org/10.1007/s00126-019-00935-y

Sillitoe RH (2015) Epithermal Paleosurfaces Miner Deposita 50:767–793. https://doi.org/10.1007/s00126-015-0614-z

Simmons SF, Christenson BW (1994) Origins of calcite in a boiling hydrothermal system. Am J Sci 294:361–400

Tămaş CG, Milési JP (2003) Hydrovolcanic breccia pipe structures—general features and genetic criteria—I. Phreatomagmatic Breccias Geologia 1:127–147. https://doi.org/10.5038/1937-8602.47.1.10

Tharalson ER, Monecke T, Reynolds TJ, Zeeck L, Pfaff K, Kelley NM (2019) The distribution of precious metals in high-grade banded quartz veins from low-sulfidation epithermal deposits: constraints from µXRF mapping. Minerals 9:740. https://doi.org/10.3390/min9120740

Vikre PG (2007) Sinter-vein correlations at Buckskin Mountain, National District, Humboldt County, Nevada. Econ Geol 102:193–224

Wallace AR (2003) Geology of the Ivanhoe Hg-Au district, northern Nevada: influence of Miocene volcanism, lakes, and active faulting on epithermal mineralization. Econ Geol 98:409–424

Walter MR, Desmarais D, Farmer JD, Hinman NW (1996) Lithofacies and biofacies of mid-Paleozoic thermal spring deposits in the Drummond Basin, Queensland, Australia. Palaios 11:497–518

Zeeck LR, Monecke T, Reynolds TJ, Tharalson ER, Pfaff K, Kelley NM, Hennigh QT (2021) Textural characteristics of barren and mineralized colloform quartz bands at the low-sulfidation epithermal deposits of the Omu Camp in Hokkaido, Japan: implications for processes resulting in bonanza-grade precious metal enrichment. Econ Geol 116:407–425. https://doi.org/10.5382/econgeo.4795

Weissberg BG (1969) Gold-silver ore-grade precipitates from New Zealand thermal waters. Econ Geol 64:95–108

White DE, Heropoulos C, Fournier RO (2001) Gold and other minor elements associated with the hot springs and geysers of Yellowstone National Park, Wyoming, Supplemented with data from Steamboat Springs, Nevada. U.S. Geologica Survey Bull2001